

---

# PACE: Post-Causal Entropy Modeling for Learned LiDAR Point Cloud Compression

---

Jiahao Zhu<sup>\*1</sup> Kang You<sup>\*2</sup> Dandan Ding<sup>1</sup> Zhan Ma<sup>2</sup>

## Abstract

LiDAR point cloud compression is vital for autonomous systems to handle massive data from high-resolution sensors. While learned entropy modeling built upon octree structures yields high compression gains, it faces two critical bottlenecks: 1) prohibitive latency, particularly during decoding, caused by causal, multi-stage context modeling; and 2) a rigid performance-latency trade-off, preventing a single model from adapting to varying constraints. These limitations stem from the tight coupling between context aggregation backbone and probability prediction. To address this, we propose PACE, a new framework that reformulates ancestral context aggregation as a non-causal backbone and confines causality to a lightweight, stage-scalable predictor, eliminating repetitive backbone executions and reducing computational overhead. The predictor supports an arbitrary number of prediction stages, supporting seamless adaptation across diverse performance-latency trade-offs without reloading parameters. Experiments demonstrate that PACE sets a new state-of-the-art in compression efficiency, achieving notable BD-BR savings and reducing decoding latency by over 90% in autoregressive mode, highly attractive for practical applications.

## 1. Introduction

Light detection and ranging (LiDAR) sensors are widely deployed in autonomous driving and robotics to capture continuous high-fidelity 3D representations (Wang et al., 2022; Qian et al., 2022; Abbasi et al., 2023; Chen et al., 2024). Outperforming passive vision sensors in range, accuracy, and illumination robustness, LiDAR is essential for localization, mapping, and obstacle detection (Lu et al., 2019;

Debeunne & Vivet, 2020; Wu et al., 2021; Li et al., 2025). Yet, the high resolution required for autonomy generates enormous data volumes, creating bottlenecks in memory, bandwidth, and computation. Consequently, efficient LiDAR point cloud compression (LPCC) is indispensable to facilitate storage, transmission, and collaborative perception (Wang et al., 2025b; Jing et al., 2026).

Octree-based methods (Zhang et al., 2024) are a cornerstone of the LPCC task, as their hierarchical partitioning effectively translates the problem of 3D geometry compression into the compression of a tree structure. Specifically, an octree recursively dissects the 3D volume into eight subspaces, representing the point cloud as a spatial tree where each level captures a finer resolution. In this structure, the geometric information of any given node is abstracted into an 8-bit occupancy code, a bitmap indicating the presence of points within its eight children. Consequently, lossless point cloud compression is equivalent to accurately modeling and entropy-coding these occupancy sequences.

Building upon this, modern learning-based approaches (Fu et al., 2022; Song et al., 2023; Jin et al., 2024; Wang et al., 2025d;c) employ deep neural networks to model level-wise occupancy dependencies, utilizing previously encoded levels as priors. Despite this shared reliance on inter-level information, they diverge in intra-level processing: i) one-stage approaches (Cui et al., 2023; You et al., 2025) rely solely on ancestor nodes from previous levels and predict all sibling nodes in the current level in one shot, achieving high parallelism with degraded coding efficiency by eliminating intra-level dependencies; ii) multi-stage frameworks (Fu et al., 2022; Wang et al., 2025c) integrate both ancestor and available sibling nodes to achieve superior compression gain, at the expense of increased computational latency.

Despite their respective advantages, both solutions exhibit inherent limitations in latency-efficiency trade-offs and adaptability, which hinder practical deployment:

- *Linear latency scaling.* Most existing multi-stage solutions adopt a fully-causal framework (see Fig. 1a), where a heavyweight backbone is repeatedly invoked for sequential processing, causing inference latency to grow linearly with the number of stages.

---

<sup>1</sup>School of Information Science and Technology, Hangzhou Normal University, Hangzhou, China <sup>2</sup>School of Electronic Science and Engineering, Nanjing University, Nanjing, China. Correspondence to: Dandan Ding <DandanDing@hznu.edu.cn>.

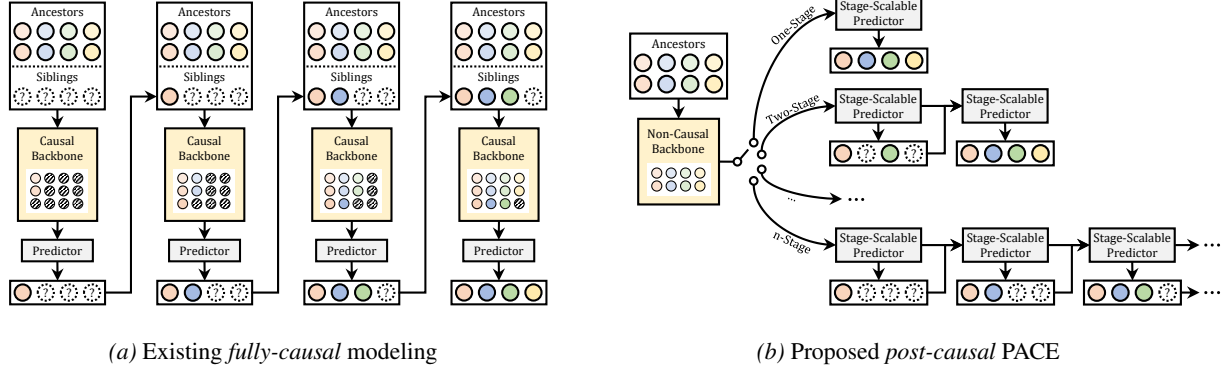


Figure 1. Octree-based LPCC paradigm. (a) Conventional fully-causal modeling, which demands repeated backbone and predictor executions due to intra-level causality constraints. (b) Proposed post-causal pipeline, which constrains causality to a lightweight and stage-scalable predictor only, reducing computational overhead and supporting dynamic stage transition.

- *Inflexible performance-latency trade-off.* Current solutions adopt fixed-stage design (e.g., one-stage or  $n$ -stage) and cannot adapt to varying resource budgets, while real applications require dynamic trade-offs between compression efficiency (e.g., archiving) and latency (e.g., interactive streaming).

To address these challenges, we propose PACE, an octree-based LPCC framework featuring a *post-causal* and *stage-scalable* entropy modeling paradigm, as illustrated in Fig. 1b. Specifically, we decouple the inter-level (i.e., ancestors) feature extraction into a non-causal backbone and impose causality only on the intra-level (i.e., siblings) prediction. By shifting causal constraints from the heavyweight backbone to the lightweight predictor, PACE eliminates repetitive backbone executions inherent in conventional fully-causal modeling, substantially reducing computational overhead. Furthermore, we devise a stage-scalable predictor with a “one-size-fits-all” capability via elastic causal embedding, which supports an arbitrary number of prediction stages with seamless transition. This enables on-the-fly reconfiguration in applications for varying performance-latency trade-offs without altering model parameters.

Extensive experiments demonstrate that PACE is remarkably effective across various stage configurations. In particular, PACE establishes new state-of-the-art across four representative datasets, including SemanticKITTI (Behley et al., 2019), Ford (Pandey et al., 2011), nuScenes (Caesar et al., 2020), and QNX (Flynn & Lasserre, 2018), achieving substantial BD-BR savings (39.01%~50.82% for one-stage and 45.14%~55.18% for multi-stage) compared to G-PCC. Notably, in autoregressive mode, PACE achieves >20% compression gains and >90% decoding latency reduction compared to a recent learning-based TopNet (Wang et al., 2025d), highlighting the effectiveness of our post-causal design. Overall, PACE offers an efficient underlying framework for LPCC, which is attractive for real applications.

The main contributions of this paper are as follows:

- We propose PACE, a post-causal entropy modeling framework that effectively decouples non-causal inter-level context aggregation from causal intra-level prediction, substantially reducing decoding overhead.
- We introduce a stage-scalable predictor with elastic causal embedding, which supports an arbitrary number of prediction stages within a single model and on-the-fly reconfiguration under dynamic constraints.
- Extensive experiments on diverse benchmarks demonstrate that PACE achieves state-of-the-art compression efficiency and significantly reduces decoding latency, validating its effectiveness and practical value.

## 2. Related Work

Learning-based LiDAR geometry compression mainly follows two routes: sparse tensor-based and octree-based methods, as introduced below.

### 2.1. Sparse Tensor-based Model

Sparse tensor represents a point cloud by partitioning 3D space into unordered voxels while skipping empty ones. By applying 3D sparse convolutions on multiscale sparse representations, methods like SparsePCGC (Wang et al., 2023), Unicorn (Wang et al., 2025a), and UniPCGC (Wang & Gao, 2025) exploit ancestry and sibling correlations, significantly outperforming the traditional G-PCC standard (WG 07 MPEG 3D Graphics Coding and Haptics Coding, 2023). However, these methods often require large kernels to handle voxel sparsity inherent in LiDAR data, increasing computational overhead. Although lightweight variants (You et al., 2025; Yu et al., 2025) accelerate inference, the local receptive fields of 3D convolutions (e.g.,  $3^3$  kernel size) limit their ability to capture long-range dependencies.

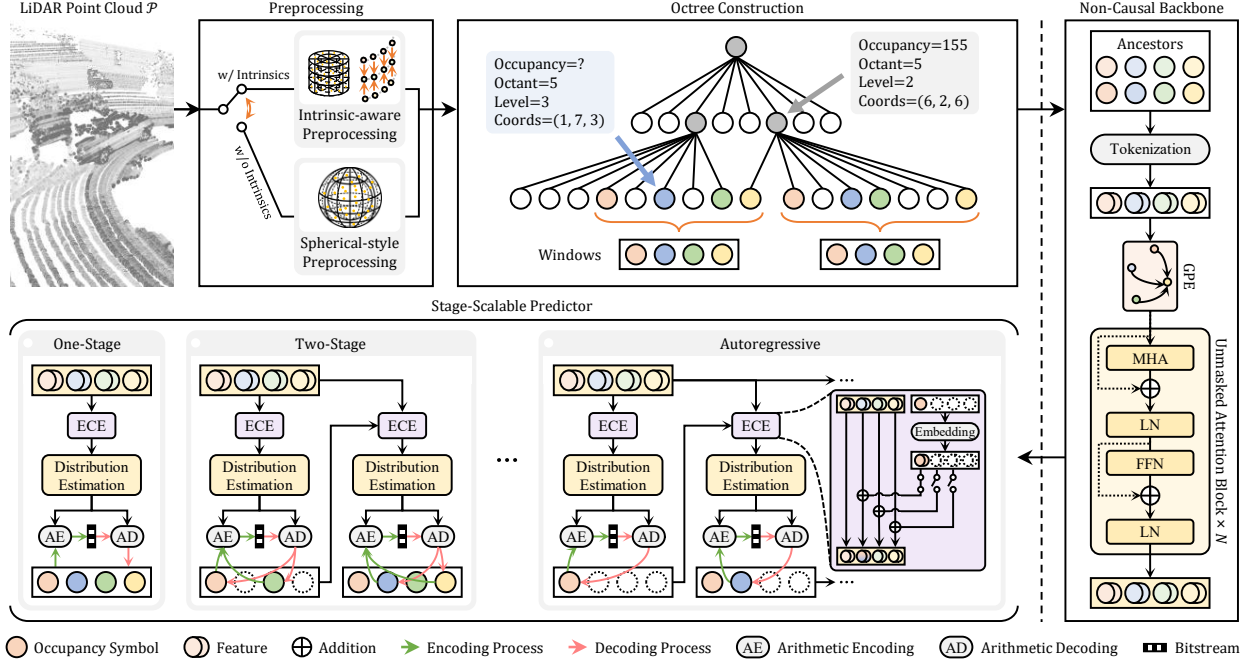


Figure 2. Framework of our proposed PACE. The LiDAR point cloud is first preprocessed for efficient octree construction, optionally using intrinsic-aware or spherical-style preprocessing depending on whether sensor intrinsics are available. Then, nodes are organized into windows for our post-causal processing: the non-causal backbone applies inter-level context aggregation, and the stage-scalable predictor exploits intra-level causality, generating the occupancy probabilities for subsequent arithmetic coding. GPE and ECE refer to the introduced graph-based positional encoding and elastic causal embedding, respectively.

## 2.2. Octree-based Model

Due to the inherent sparsity of LiDAR scans, a serialized approach is more conducive to modeling contextual information, as demonstrated in perception tasks (Wu et al., 2024; Jin et al., 2025). Thus, octree-based representations have emerged as a popular paradigm for learned LPCC.

**One-stage approach.** Previous efforts such as OctSqueeze (Huang et al., 2020) and OctFormer (Cui et al., 2023) focus on ancestor-to-child dependencies. By discarding sibling contexts, they implement high-speed parallel decoding. However, the absence of intra-level dependencies results in suboptimal compression gains.

**Autoregressive approach.** To improve the coding performance, OctAttention (Fu et al., 2022) introduces sibling dependencies via masked attention, predicting node status on a node-by-node basis. This paradigm is further refined by TopNet (Wang et al., 2025d) and ASRL (Wang et al., 2025c), which utilize convolution-enhanced or sparsity-aware attention to capture long-range dependencies. Despite superior compression performance, their strict serial dependency forces re-executing the heavy backbone for each node, causing prohibitive decoding latency.

**Multi-stage approach.** To balance compression efficiency and computational cost, EHEM (Song et al., 2023) and ECM-OPCC (Jin et al., 2024) devise multi-stage context

modeling, partitioning nodes into disjoint sets and decoding them stage by stage. GAEM (Cui et al., 2025) further utilizes graph-driven attention in context aggregation to capture structural correlations. Despite improving R-D performance, they are constrained by a rigid coupling between context aggregation backbone and prediction head: the backbone must be re-executed for each stage, and the performance-latency trade-off is fixed once the model is trained.

**In summary,** one-stage models prioritize low latency but sacrifice compression gains, whereas multi-stage and autoregressive models achieve higher gains at the cost of linearly increased decoding latency. A robust paradigm that overcomes this limitation while offering flexible performance-latency trade-offs remains an open challenge.

## 3. Methodology

The framework of PACE is illustrated in Fig. 2, consisting of three stages: octree construction using intrinsic-aware or spherical-style preprocessing, non-causal backbone for inter-level context aggregation, and stage-scalable predictor to predict the occupancy distribution for entropy coding.

### 3.1. Intrinsic-aware Preprocessing

Let  $\mathcal{P} = \{(x_i, y_i, z_i)\}_{i=1}^N$  be the input LiDAR point cloud, where each point  $(x_i, y_i, z_i)$  represents the Cartesian co-

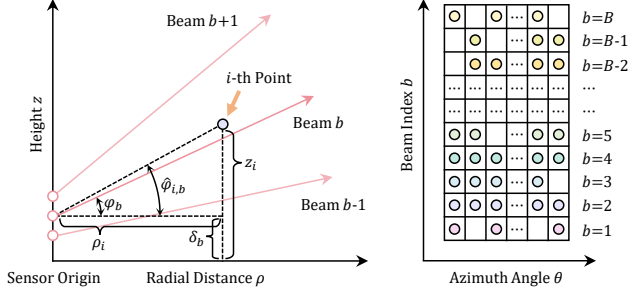


Figure 3. Beam index mapping. Left: The  $i$ -th point is mapped to a discrete beam by minimizing the angular residual between its theoretical pitch  $\hat{\varphi}_{i,b}$  and calibrated pitch  $\varphi_b$ . Right: The structured hybrid cylindrical-beam representation, offering a more hardware-aligned alternative to standard cylindrical projections.

ordinates. Unlike prior methods that directly project Cartesian coordinates  $(x_i, y_i, z_i)$  into a cylindrical system  $(\rho_i, \theta_i, z_i)$  (Gao et al., 2023), we further utilize sensor intrinsics (e.g., laser pitch angles and vertical offsets) to map the vertical component  $z_i$  to a discrete beam index  $b_i$ , yielding a hybrid cylindrical-beam representation  $(\rho_i, \theta_i, b_i)$ . The discretization of  $b_i$  inherently reduces representation complexity, and can be reversed via sensor calibration during decoding to recover the original  $z_i$  coordinates.

**Cylindrical coordinate conversion.** We first convert the input point cloud from Cartesian coordinates  $(x_i, y_i, z_i)$  to cylindrical coordinates  $(\rho_i, \theta_i, z_i)$  via:

$$\rho_i = \sqrt{x_i^2 + y_i^2}, \theta_i = \arctan\left(\frac{y_i}{x_i}\right), \text{ and } z_i = z_i, \quad (1)$$

where  $\rho_i$  and  $\theta_i$  refer to the radial distance (or planar distance) and the azimuth angle of the  $i$ -th point, respectively.

**Beam index mapping.** Define the sensor intrinsics by the laser pitch angles  $\Phi = \{\varphi_b\}_{b=1}^B$  and per-beam vertical offsets  $\Delta = \{\delta_b\}_{b=1}^B$ , where  $B$  denotes the total number of laser beams (e.g., 32 or 64) and  $b$  is the beam index. As depicted in Fig. 3, for each point, we calculate the theoretical pitch angle corresponding to the  $b$ -th beam, mathematically:

$$\hat{\varphi}_{i,b} = \arctan\left(\frac{z_i - \delta_b}{\rho_i}\right), \forall b \in \{1, \dots, B\}. \quad (2)$$

The point is then assigned to the beam index  $b_i$  that minimizes the angular residual, i.e.,

$$b_i = \operatorname{argmin}_{b \in \{1, \dots, B\}} \|\hat{\varphi}_{i,b} - \varphi_b\|_2^2. \quad (3)$$

This yields the cylindrical-beam representation  $(\rho_i, \theta_i, b_i)$ , which is used in PACE to construct an octree structure. However, in scenarios where accurate intrinsics are unavailable (e.g., the LiDAR scans in SemanticKITTI (Behley et al., 2019)), we adopt a standard multi-level spherical processing following the previous work (Luo et al., 2024), thereby ensuring applicability across diverse datasets.

## 3.2. Octree-based Deep Entropy Model

**Octree representation.** Building upon the intrinsic-aware coordinate transformation, the point cloud is discretized into a hierarchical multi-level octree structure. Let  $L$  denote the maximum octree depth. For any given level  $l \in \{1, \dots, L\}$ , the occupancy sequence  $\mathcal{O}^l$  is derived by collecting all non-empty nodes via breadth-first traversal:

$$\mathcal{O}^l = \{o_1^l, o_2^l, \dots, o_{N_l}^l\}, \quad (4)$$

where  $o_i^l \in \{1, \dots, 255\}$  represents the occupancy symbol of the  $i$ -th node at level  $l$ , and  $N^l$  denotes the total number of nodes at this level. Consequently, the complete geometry of the LiDAR scan is encapsulated by the concatenated level-wise occupancy sequences, denoted as  $\mathcal{O} = \{\mathcal{O}^1, \dots, \mathcal{O}^L\}$ .

**Probabilistic entropy modeling.** To compress the occupancy sequence  $\mathcal{O}$ , a deep parametric model is constructed to approximate the probability distribution  $p(\mathcal{O})$ . Theoretically, minimizing the compression bitrate  $\mathcal{R}$  is equivalent to minimizing the cross-entropy between the estimated distribution  $p(\mathcal{O})$  and the actual distribution  $q(\mathcal{O})$ :

$$\mathcal{R} = \mathbb{E}_{\mathcal{O} \sim q(\mathcal{O})} [-\log_2 p(\mathcal{O})]. \quad (5)$$

To effectively model the complex dependencies within the octree, the probability  $p(\mathcal{O})$  is factorized into a coarse-to-fine chain, which incorporates two dependency paradigms:

i) *Inter-level prediction* utilizes ancestral information from coarser levels ( $\mathcal{O}^{<l}$ ) to progressively predict the occupancy distribution of the current level  $l$ :

$$p(\mathcal{O}) = \prod_{l=1}^L p(\mathcal{O}^l | \mathcal{O}^{<l}). \quad (6)$$

ii) *Intra-level prediction* decomposes the current level into  $S$  stages, denoted as  $\mathcal{O}^l = \{\mathcal{O}_1^l, \dots, \mathcal{O}_S^l\}$ , and predicts the current stage conditioned on the preceding ones:

$$\begin{aligned} p(\mathcal{O}^l | \mathcal{O}^{<l}) &= p(\mathcal{O}_1^l, \mathcal{O}_2^l, \dots, \mathcal{O}_S^l | \mathcal{O}^{<l}), \\ &= p(\mathcal{O}_1^l | \mathcal{O}^{<l}) \prod_{s=2}^S p(\mathcal{O}_s^l | \mathcal{O}_{<s}^l, \mathcal{O}^{<l}). \end{aligned} \quad (7)$$

**Remark.** In deep entropy models, inter-level dependencies are strictly dictated by the octree’s hierarchical structure. Therefore, this work concentrates on intra-level stage-wise causality (i.e., the sequential dependencies between different stages) in multi-stage (including autoregressive) processing.

## 3.3. Non-Causal Backbone

Unlike prior works that fuse inter-level ( $\mathcal{O}^{<l}$ ) and intra-level ( $\mathcal{O}_{<s}^l$ ) contexts before the causal backbone (either via raw occupancy symbols (Fu et al., 2022; Wang et al., 2025d) or feature representations (Song et al., 2023; Luo et al., 2024)), we propose to aggregate inter-level context using a non-causal backbone and introduce interaction between inter- and intra-level contexts within a lightweight predictor.

**Window partition.** To facilitate efficient attention-based feature interaction, the occupancy sequence  $\mathcal{O}^l$  at level  $l$  is partitioned into non-overlapping windows of size  $W$ . Specifically, the  $m$ -th window  $\mathcal{O}^{l,m}$  is defined as:

$$\mathcal{O}^{l,m} = \{o_i^l \mid (m-1)W < i \leq mW\}. \quad (8)$$

The superscripts  $l$  and  $m$  are omitted in the following for brevity since subsequent operations are performed independently within each window.

**Context tokenization.** For  $i$ -th octree node in the window, we first project its inter-level context into a vectorized token  $e_i$ , which fuses the octant  $t_i$ , the level  $l$ , and the embeddings of  $G$  generations of ancestors  $\{o_i^{(g)}\}_{g=1}^G$ :

$$e_i = \left( \bigoplus_{g=1}^G \text{Emb}(o_i^{(g)}) \right) \oplus \text{Emb}(t_i) \oplus \text{Emb}(l), \quad (9)$$

where  $\text{Emb}(\cdot)$  denotes the embedding layer (implemented as a learnable lookup table);  $\text{MLP}(\cdot)$  means multi-layer perceptron;  $\oplus$  denotes concatenation. We empirically set  $G$  to 3 in our experiments.

**Graph-based positional encoding.** We introduce graph-based positional encoding (GPE) to explicitly incorporate 3D structural priors in our backbone. Specifically, for each node  $i$ , let  $\mathbf{c}_i \in [-1, 1]$  denote its normalized coordinates<sup>1</sup>, we first fuse the context token  $e_i$  with the coordinates  $\mathbf{c}_i$ :

$$e'_i = \text{MLP}(e_i) + \text{MLP}(\mathbf{c}_i). \quad (10)$$

To capture local dependencies, we construct a  $k$ -NN graph  $\mathcal{N}(i)$  and compute edge features  $e'_j$  via an EdgeConv (Wang et al., 2019) variant, encoding the interaction between node  $i$  and its spatial neighbors  $j \in \mathcal{N}(i)$ :

$$e''_j = \text{MLP}(e'_i \oplus (e'_j - e'_i)). \quad (11)$$

Finally, neighborhood information is aggregated through a gated mechanism:

$$\bar{e}_i = \text{MAX}_{j \in \mathcal{N}(i)} \{ \text{MLP}(e''_j \odot \text{Gate}(e''_j)) \}, \quad (12)$$

where  $\text{Gate}(\cdot)$  denotes a Linear layer with SiLU activation;  $\odot$  means the Hadamard product;  $\text{MAX}$  performs channel-wise max-pooling over the local neighborhood  $j \in \mathcal{N}(i)$ .

**Unmasked Attention.** Following GPE, we apply unmasked scaled dot-product attention within each window, as shown on the right of Fig. 2. Specifically, let the input feature be  $\mathcal{A}^{(0)} = \{\bar{e}_i\}_{i=1}^W$ , then the updated feature  $\mathcal{A}^{(i+1)}$  is computed by querying all nodes within the window:

$$\tilde{\mathcal{A}}^{(i)} = \text{LayerNorm} \left( \mathcal{A}^{(i)} + \text{MHA}(\mathcal{A}^{(i)}) \right), \quad (13)$$

$$\mathcal{A}^{(i+1)} = \text{LayerNorm} \left( \tilde{\mathcal{A}}^{(i)} + \text{FFN}(\tilde{\mathcal{A}}^{(i)}) \right), \quad (14)$$

<sup>1</sup>Depending on the availability of intrinsics, the coordinates are represented either as  $(\rho_i, \theta_i, b_i)$  or as spherical coordinates.

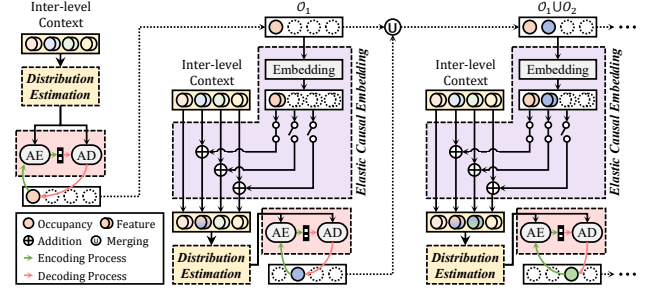


Figure 4. Stage-scalable predictor. The inter-level context yielded by the non-causal backbone is shared across all stages, and the intra-level context ( $O_{<s}$ ,  $s \in [1, S]$ ) from previous stages is embedded and fused to predict the target stage  $O_s$ . The autoregressive mode is presented as an illustrative example.

where  $\text{MHA}(\cdot)$  and  $\text{FFN}(\cdot)$  denote multi-head attention and a feed-forward network, respectively. By stacking  $N$  such layers, the final refined feature serves as the non-causal inter-level context for the subsequent stage-scalable predictor.

### 3.4. Stage-Scalable Predictor

Building upon the non-causal backbone that extracts inter-level context, we introduce a stage-scalable predictor with flexible stage-wise causality, achieving dynamic trade-offs between compression efficiency and computational latency.

**Stage-wise decomposition.** Given a window of occupancy symbols  $\mathcal{O} = \{o_i\}_{i=1}^W$  and corresponding inter-level context  $\mathcal{A} = \{\mathbf{a}_i\}_{i=1}^W$ , we uniformly partition  $\mathcal{O}$  into  $S$  stages via:

$$\mathcal{O}_s = \{o_{k \times S + s} \mid k \times S + s \leq W, k \in \mathbb{N}_0\}. \quad (15)$$

By varying  $S$ , the predictor can span a spectrum of coding paradigms. E.g., when  $S=1$ , the entire window is treated as a single stage  $\mathcal{O}_1 = \{o_i\}_{i=1}^W$  for fully parallel processing; when  $S=W$ , each stage contains exactly one node, i.e.,  $\mathcal{O}_s = \{o_s\}$ , resulting in a fully autoregressive mode. We transmit  $S$  to the decoder for consistent stage decomposition.

**Elastic causal embedding.** As shown in Fig. 4, for each node  $i$  in the  $s$ -th stage, we fuse the inter-level context  $\mathbf{a}_i$  with the preceding context from previous stages  $\mathcal{O}_{<s}$ :

$$\mathbf{f}_i^{(s)} = \mathbf{a}_i + \mathbb{I}(o_{i-1} \in \bigcup \mathcal{O}_{<s}) \cdot \text{Emb}(o_{i-1}), \quad (16)$$

where the indicator function  $\mathbb{I}(\cdot)$  ensures that sibling  $o_{i-1}$  is only utilized if it was decoded in a preceding stage. Note that when  $s=1$ ,  $\mathbf{f}_i^{(s)}$  is equivalent to  $\mathbf{a}_i$ , as the set of preceding stages  $\mathcal{O}_{<s}$  is empty.

**Distribution estimation.** To capture local dependencies within the fused features  $\mathcal{F}^{(s)} = \{\mathbf{f}_i^{(s)}\}_{i=1}^W$ , we employ a Selective State Space Model (SSM) instantiated by a Mamba (Gu & Dao, 2023) block. The SSM facilitates efficient context aggregation across the sequence:

$$\tilde{\mathcal{F}}^{(s)} = \text{SSM}(\mathcal{F}^{(s)}). \quad (17)$$

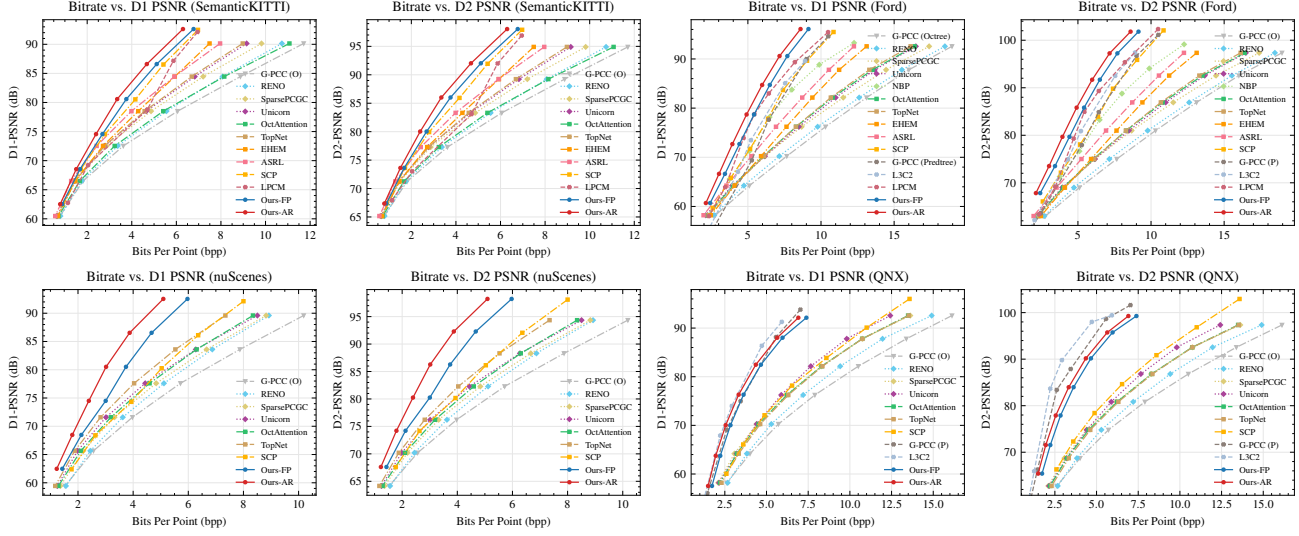


Figure 5. Comparison of rate-distortion (R-D) performance across SemanticKITTI, Ford, nuScenes, and QNX datasets. G-PCC (O) and G-PCC (P) represent the Octree and Predgeom configurations of G-PCC, respectively.

The occupancy distribution for each symbol  $o_i \in \mathcal{O}_s$  is then estimated via  $\tilde{\mathbf{f}}_i^{(s)} \in \tilde{\mathcal{F}}^{(s)}$ :

$$p(o_i) = \text{Softmax} \left( \text{MLP} \left( \tilde{\mathbf{f}}_i^{(s)} \right) \right), \quad (18)$$

where  $p(o_i)$  serves as the categorical distribution for the arithmetic coder to compress  $o_i$ .

## 4. Experiment and Analysis

### 4.1. Experimental Settings

**Datasets.** We evaluate the performance of PACE on four representative datasets: SemanticKITTI (Behley et al., 2019), Ford (Pandey et al., 2011), nuScenes (Caesar et al., 2020), and QNX (Flynn & Lasserre, 2018).

- **SemanticKITTI** is acquired using a Velodyne HDL-64E LiDAR sensor and comprises 22 point cloud sequences with a total of 43,504 frames. Each frame contains about 120k points. Following prior works (Song et al., 2023; Wang et al., 2025d), sequences #00~#10 are used for training and #11~#21 for testing.
- **Ford** is also collected using a Velodyne HDL-64E LiDAR sensor. Under the common test condition (CTC) defined by MPEG G-PCC (WG 07 MPEG 3D Graphics Coding and Haptics Coding, 2024), three Ford sequences are used, each having 1,500 frames at 1 mm precision. The first sequence is used for training and the other two for testing.
- **nuScenes** is a large-scale autonomous driving dataset collected via a Velodyne HDL-32E LiDAR sensor. We select 6,000 frames for training and 450 for testing.

- **QNX** is a LiDAR dataset recommended by the MPEG G-PCC CTC, collected using a Velodyne VLP16 sensor at 1 mm precision. It contains four sequences with approximately 30k points per frame. Two sequences are used for training and the remaining two for testing.

All samples are voxelized following prior works (Song et al., 2023; Luo et al., 2024). Specifically, we set the quantization depth to  $L=16$  for raw SemanticKITTI and nuScenes, with scaling factors of  $\frac{400}{2^{L-1}}$  and  $\frac{450}{2^{L-1}}$ , respectively. Ford and QNX are already voxelized at 1 mm precision. We vary  $L$  to evaluate the model across different bitrates.

**Baseline Methods.** We compare PACE against existing LPCC methods: rules-based MPEG G-PCC (WG 07 MPEG 3D Graphics Coding and Haptics Coding, 2023) TMC13v23 (Octree and Predgeom) and TMLv4 (a.k.a. L3C2 (Sébastien & Jonathan, 2021)); multiscale sparse tensor-based methods RENO (You et al., 2025), SparsePCGC (Wang et al., 2023), Unicorn (Wang et al., 2025a), and NBP (Liu et al., 2026); octree-based methods OctAttention (Fu et al., 2022), TopNet (Wang et al., 2025d), EHEM (Song et al., 2023), ASRL (Wang et al., 2025c), and SCP (Luo et al., 2024); predtree-based method LPCM (Sun et al., 2025). All methods are evaluated under identical conditions.

**Evaluation Metrics.** We use point-to-point (D1) and point-to-plane (D2) PSNR to measure distortion and bits per point (bpp) to measure bitrate. PSNR peak values are set to 59.70 for SemanticKITTI and nuScenes and 30,000 for Ford and QNX. The Bjøntegaard Delta Bitrate (BD-BR) (Bjøntegaard, 2001) is used to assess rate-distortion (R-D) performance, which quantifies the average bitrate change between two codecs at equivalent objective quality, where lower is better.

Table 1. Compression performance comparison. BD-BR (%) is reported against the G-PCC (Octree) anchor. Ours-FP and Ours-AR denote our fully parallel (one-stage) and autoregressive modes, respectively. The top three results are highlighted as **first**, **second** and **third**.

METHOD	PUB.	KITTI		FORD		NUScENES		QNX	
		D1 ↓	D2 ↓	D1 ↓	D2 ↓	D1 ↓	D2 ↓	D1 ↓	D2 ↓
<i>Sparse tensor-based models</i>									
RENO	CVPR 2025	-06.21%	-06.20%	-05.02%	-05.02%	-08.53%	-08.58%	-07.62%	-07.64%
SPARSEPCGC	TPAMI 2023	-18.64%	-18.63%	-16.08%	-16.08%	-14.84%	-14.86%	-21.40%	-21.40%
UNICORN	TPAMI 2025	-22.26%	-22.26%	-18.51%	-18.50%	-21.55%	-21.56%	-23.84%	-23.86%
NBP	TPAMI 2026	N/A	N/A	-39.71%	-41.19%	N/A	N/A	N/A	N/A
<i>Octree-based models</i>									
OCTATTENTION	AAAI 2022	-08.93%	-08.93%	-18.97%	-18.97%	-18.90%	-18.92%	-19.90%	-19.91%
TOPNET	CVPR 2025	-22.58%	-22.57%	-18.77%	-18.77%	-28.20%	-28.22%	-18.59%	-18.60%
EHEM	CVPR 2023	-26.44%	-26.41%	-24.60%	-24.60%	N/A	N/A	N/A	N/A
ASRL	SPL 2025	-31.98%	-31.97%	-32.43%	-32.43%	N/A	N/A	N/A	N/A
SCP	AAAI 2024	-35.72%	-37.87%	-40.26%	-44.45%	-20.67%	-25.42%	-22.66%	-29.58%
<i>Predtree-based models</i>									
G-PCC (PREEDGEOM)	MPEG 2023	N/A	N/A	-45.24%	-48.53%	N/A	N/A	-53.21%	-66.15%
L3C2	MPEG 2025	N/A	N/A	-45.67%	-50.06%	N/A	N/A	-57.76%	-71.57%
LPCM	ArXiv 2025	-28.91%	-25.94%	-48.30%	-50.07%	N/A	N/A	N/A	N/A
OURS-FP	This Paper	-39.01%	-41.00%	-50.19%	-55.02%	-39.77%	-42.91%	-50.82%	-57.86%
OURS-AR	This Paper	-45.14%	-46.97%	-55.07%	-59.51%	-50.38%	-52.95%	-55.18%	-61.73%

**Implementation Details.** We train our models using the AdamW optimizer (Loshchilov & Hutter, 2019) with an initial learning rate of  $5 \times 10^{-4}$ . The training duration varies by dataset: 10 epochs for SemanticKITTI and QNX, 25 epochs for nuScenes, and 50 epochs for Ford. All experiments are conducted on a workstation equipped with an NVIDIA RTX 4090 GPU and an Intel i9-13900K CPU.

### 4.2. Performance Evaluation

Figure 5 and Table 1 present the BD-BR performance of various methods across four datasets. Under both one-stage mode (i.e., fully parallel mode, termed Ours-FP) and the autoregressive mode (Ours-AR), PACE consistently ranks as the top or top performer across all datasets and distortion metrics, demonstrating a clear advantage over both traditional rules-based and learning-based approaches. While recent octree-based models (e.g., TopNet (Wang et al., 2025d), EHEM (Song et al., 2023), and SCP (Luo et al., 2024)) already surpass the G-PCC (Octree) baseline, PACE further improves BD-BR by a substantial margin.

Note that rules-based predtree models are restricted to scans with LiDAR intrinsics, as prediction tree construction relies heavily on these parameters. Thus, they apply only to intrinsics-available datasets such as Ford and QNX, often outperforming octree-based models. However, by incorporating intrinsic-aware preprocessing, PACE equips the octree with the ability of leveraging intrinsic data, leading to significant compression improvements in these scenarios. For example, PACE attains comparable gains with G-PCC (Predgeom) and L3C2 on QNX and surpasses them on Ford. PACE also outperforms LPCM, a learned predtree method.

Table 2. Complexity comparison. We compare our method against open-source octree-based baselines in terms of model size, memory usage, and runtime (encoding/decoding) at octree level  $L=14$ .

METHOD	PARAM. ↓	MEM. ↓	ENC. ↓	DEC. ↓
OCTATTENTION	4.23M	0.31GB	2.40s	282.04s
TOPNET	3.37M	0.30GB	2.46s	290.26s
SCP	24.51M	1.08GB	8.94s	9.01s
OURS-FP	10.57M	0.58GB	1.72s	1.55s
OURS-AR	10.57M	0.58GB	10.89s	16.36s

### 4.3. Complexity Comparison

PACE complements its R-D gains with affordable computational complexity. As presented in Table 2, the one-stage mode (Ours-FP) achieves an optimal speed-performance trade-off, delivering higher compression accuracy while outperforming competing methods in both encoding and decoding speeds. Furthermore, the autoregressive mode (Ours-AR) reduces decoding latency by over 90% compared to existing autoregressive models such as OctAttention and TopNet, a leap attributed to our post-causal design.

Currently, our implementation remains a prototype with encoding-time overhead in AR mode as the main bottleneck (10.89 s). In principle, as all information is available during encoding, the stage-scalable predictor can be parallelized to further improve speed (theoretically comparable to the FP mode), which we leave for our future work.

### 4.4. Ablation Study

Ablation studies evaluate the contribution of each component using the Ford dataset recommended by MPEG CTC.

**Preprocessing.** LiDAR’s mechanical scanning often requires preprocessing (e.g., coordinate transformation) to optimize octree representation for higher compression gains. For instance, SCP (Luo et al., 2024) uses a spherical-coordinate-based octree. We evaluate PACE across various preprocessing methods in Fig. 6. As observed, the SCP scheme (labeled “Sph.”) surpasses the direct octree construction in the Cartesian coordinate system (labeled “Cart.”). Further, our intrinsic-aware approach achieves the best performance through better leveraging sensor intrinsics.

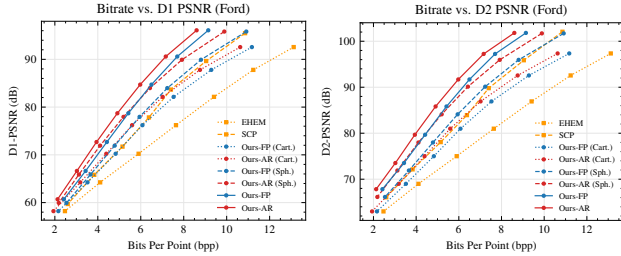


Figure 6. Ablation on preprocessing methods. “Sph.” and “Cart.” denote spherical- and Cartesian-based octrees, respectively.

**Fully-causal vs. Post-causal modeling.** The strategy of concatenating ancestors and siblings before a masked backbone (termed fully-causal modeling) remains a common practice in existing works (Wang et al., 2025d;c). We implement this strategy in PACE for comparison. Figure 7 illustrates that the fully-causal PACE suffers from high decoding latency due to repeated backbone computations (e.g.,  $\sim 90\times$  slower at level  $L=14$ ), and its masking scheme causes information loss by occluding ancestral features, resulting in inferior performance compared to the post-causal version (-52.34% vs. -55.07%). In addition, the post-causal pipeline allows on-the-fly reconfiguration of prediction stages. For instance, a single trained PACE model can be directly applied to any number of stages without parameter reloading. Conversely, the fully-causal model must be specifically re-trained for each new configuration, greatly increasing storage and computational overhead.

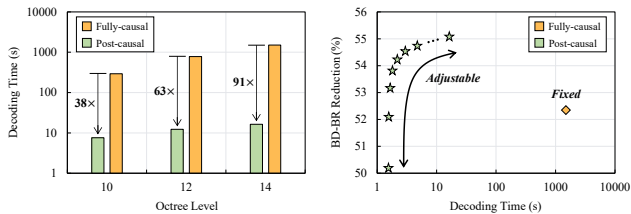


Figure 7. Evaluation of fully-causal and post-causal modeling. Left: Decoding latency comparison in the autoregressive (AR) mode of PACE. Right: Efficiency-complexity Pareto front, where complexity is measured as decoding time at octree level 14.

**Graph-based positional encoding (GPE).** Table 3 evaluates the impact of GPE. Notably, GPE adds negligible

overhead while consistently improving compression: BD-BR reduction is improved from -38.22% to -50.19% in our FP mode and from -46.14% to -55.07% in our AR mode. These results suggest that modeling 3D geometric relations via graphs effectively complements the serialized octree order, yielding more informative context.

Table 3. Ablation study on graph-based positional encoding

CONFIG	OURS-FP		OURS-AR	
	PARAM. ↓	BD-BR ↓	PARAM. ↓	BD-BR ↓
w/o GPE	10.24M	-38.22%	10.24M	-46.14%
w/ GPE	10.57M	-50.19%	10.57M	-55.07%

**Stage-scalable prediction.** To evaluate the flexibility and efficiency of our stage-scalable predictor, we analyze the performance-latency trade-offs by varying the number of stages  $S$  during inference. As illustrated in Table 4, increasing  $S$  from 1 to 16 consistently enhances BD-BR performance (from -50.19% to -54.23%) by capturing denser intra-level dependencies. Notably, as our post-causal design executes the heavy backbone only once, the computational overhead grows only marginally, with decoding time increasing from 1.55 s to 2.18 s from 1-stage to 16-stage. Although the fully autoregressive variant achieves the best BD-BR (-55.07%), it suffers from longer decoding latency due to the node-by-node prediction; therefore, it mainly serves as an upper-bound reference. In practical applications, the number of stages in PACE can be dynamically configured for balanced trade-offs.

Table 4. On-the-fly reconfiguration of prediction stages in PACE

CONFIG	MEM. ↓	ENC. ↓	DEC. ↓	BD-BR ↓
1-STAGE	0.58GB	<b>1.72s</b>	<b>1.55s</b>	-50.19%
2-STAGE	0.58GB	1.76s	1.57s	-52.09%
4-STAGE	0.58GB	1.81s	1.66s	-53.16%
8-STAGE	0.58GB	1.94s	1.80s	-53.81%
16-STAGE	0.58GB	2.20s	2.18s	-54.23%
AUTOREGRESSIVE	0.58GB	10.89s	16.36s	<b>-55.07%</b>

## 5. Conclusion

This paper introduces PACE, an LPCC framework addressing the rigid trade-off between compression gain and computational overhead via a post-causal paradigm. By decoupling inter-level context aggregation into a non-causal backbone and restricting causality to a stage-scalable predictor, we eliminate redundant computations and improve compression gains. Under the post-causal paradigm, PACE achieves state-of-the-art efficiency across four benchmarks while reducing decoding latency by over 90% in autoregressive mode. For practical deployment, our PACE offers the flexibility required by real systems and supports seamless adaptation to varying performance-latency constraints.

## Impact Statement

This paper presents work whose goal is to advance the field of Machine Learning. There are many potential societal consequences of our work, none which we feel must be specifically highlighted here.

## References

- Abbasi, R., Bashir, A. K., Alyamani, H. J., Amin, F., Doh, J., and Chen, J. LiDAR point cloud compression, processing and learning for autonomous driving. *IEEE Transactions on Intelligent Transportation Systems*, 24(1):962–979, 2023.
- Behley, J., Garbade, M., Milioto, A., Quenzel, J., Behnke, S., Stachniss, C., and Gall, J. SemanticKITTI: A dataset for semantic scene understanding of LiDAR sequences. *2019 IEEE/CVF International Conference on Computer Vision (ICCV)*, pp. 9296–9306, 2019.
- Bjontegaard, G. Calculation of average PSNR differences between rd-curves. In *ITU-T SG 16/Q6, 13th VCEG Meeting*. document VCEG-M33, April 2001.
- Caesar, H., Bankiti, V., Lang, A. H., Vora, S., Liong, V. E., Xu, Q., Krishnan, A., Pan, Y., Baldan, G., and Beijbom, O. nuScenes: A multimodal dataset for autonomous driving. In *Proceedings of the IEEE/CVF Conference on Computer Vision and Pattern Recognition*, pp. 11621–11631, 2020.
- Chen, L., Wu, P., Chitta, K., Jaeger, B., Geiger, A., and Li, H. End-to-end autonomous driving: Challenges and frontiers. *IEEE Transactions on Pattern Analysis and Machine Intelligence*, 46(12):10164–10183, 2024.
- Cui, M., Long, J., Feng, M., Li, B., and Kai, H. OctFormer: Efficient octree-based transformer for point cloud compression with local enhancement. In *Proceedings of the AAAI Conference on Artificial Intelligence*, volume 37, pp. 470–478, 2023.
- Cui, M., Zhong, Y., Feng, M., Long, J., Ling, Y., Xu, J., and Huang, K. GAEM: Graph-driven attention-based entropy model for LiDAR point cloud compression. *IEEE Transactions on Circuits and Systems for Video Technology*, 35(9):9105–9118, 2025.
- Debeunne, C. and Vivet, D. A review of visual-LiDAR fusion based simultaneous localization and mapping. *Sensors*, 20(7), 2020. ISSN 1424-8220.
- Flynn, D. and Lasserre, S. PCC Cat3 test sequences from BlackBerry—QNX. input document m23647, ISO/IEC JTC1/SC29/WG11, July 2018.
- Fu, C., Li, G., Song, R., Gao, W., and Liu, S. OctAttention: Octree-based large-scale contexts model for point cloud compression. In *Proceedings of the AAAI conference on artificial intelligence*, volume 36, pp. 625–633, 2022.
- Gao, Y., Zhang, P., and Wang, X. Lossy LiDAR point cloud compression via cylindrical 3D convolution networks. In *2023 IEEE International Conference on Image Processing (ICIP)*, pp. 3508–3512, 2023.
- Gu, A. and Dao, T. Mamba: Linear-time sequence modeling with selective state spaces. *arXiv preprint arXiv:2312.00752*, 2023.
- Huang, L., Wang, S., Wong, K., Liu, J., and Urtasun, R. OctSqueeze: Octree-structured entropy model for LiDAR compression. In *Proceedings of the IEEE/CVF Conference on Computer Vision and Pattern Recognition*, pp. 1313–1323, 2020.
- Jin, X., Su, H., Liu, K., Ma, C., Wu, W., Hui, F., and Yan, J. UniMamba: Unified spatial-channel representation learning with group-efficient mamba for LiDAR-based 3D object detection. In *Proceedings of the Computer Vision and Pattern Recognition Conference*, pp. 1407–1417, 2025.
- Jin, Y., Zhu, Z., Xu, T., Lin, Y., and Wang, Y. ECM-OPCC: Efficient context model for octree-based point cloud compression. In *ICASSP 2024-2024 IEEE International Conference on Acoustics, Speech and Signal Processing (ICASSP)*, pp. 7985–7989, 2024.
- Jing, H., Wang, A., Zhang, Y., Bu, D., and Hou, J. Reflectance prediction-based knowledge distillation for robust 3D object detection in compressed point clouds. *IEEE Transactions on Image Processing*, 35:85–97, 2026.
- Li, Z., Wang, W., Li, H., Xie, E., Sima, C., Lu, T., Yu, Q., and Dai, J. BEVFormer: Learning bird’s-eye-view representation from LiDAR-camera via spatiotemporal transformers. *IEEE Transactions on Pattern Analysis and Machine Intelligence*, 47(3):2020–2036, 2025.
- Liu, B., Ma, Y., Li, L., Liu, D., Li, Z., and Li, H. Next bit prediction: A unified lossless and lossy point cloud geometry compression framework. *IEEE Transactions on Pattern Analysis and Machine Intelligence*, pp. 1–18, 2026.
- Loshchilov, I. and Hutter, F. Decoupled weight decay regularization. In *7th International Conference on Learning Representations, ICLR 2019*, 2019.
- Lu, W., Zhou, Y., Wan, G., Hou, S., and Song, S. L3-Net: Towards learning based LiDAR localization for autonomous driving. In *Proceedings of the IEEE/CVF Conference on Computer Vision and Pattern Recognition (CVPR)*, June 2019.

- Luo, A., Song, L., Nonaka, K., Unno, K., Sun, H., Goto, M., and Katto, J. SCP: Spherical-coordinate-based learned point cloud compression. In *Proceedings of the AAAI Conference on Artificial Intelligence*, volume 38, pp. 3954–3962, 2024.
- Pandey, G., McBride, J. R., and Eustice, R. M. Ford campus vision and LiDAR data set. *International Journal of Robotics Research*, 30(13):1543–1552, 2011.
- Qian, R., Lai, X., and Li, X. 3D object detection for autonomous driving: A survey. *Pattern Recognition*, 130: 108796, 2022. ISSN 0031-3203.
- Sébastien, L. and Jonathan, T. A point cloud codec for LiDAR data with very low complexity and latency. *ISO/IEC JTC1/SC29/WG07 MPEG*, 2021.
- Song, R., Fu, C., Liu, S., and Li, G. Efficient hierarchical entropy model for learned point cloud compression. In *Proceedings of the IEEE/CVF Conference on Computer Vision and Pattern Recognition*, pp. 14368–14377, 2023.
- Sun, C., Yuan, H., Jiang, S., Ai, D., Zhang, W., and Hamzaoui, R. LPCM: Learning-based predictive coding for LiDAR point cloud compression. *arXiv preprint arXiv:2505.20059*, 2025.
- Wang, G., Wu, X., Jiang, S., Liu, Z., and Wang, H. Efficient 3D deep LiDAR odometry. *IEEE Transactions on Pattern Analysis and Machine Intelligence*, 45(5):5749–5765, 2022.
- Wang, J., Ding, D., Li, Z., Feng, X., Cao, C., and Ma, Z. Sparse tensor-based multiscale representation for point cloud geometry compression. *IEEE Transactions on Pattern Analysis and Machine Intelligence*, 45(7):9055–9071, 2023.
- Wang, J., Xue, R., Li, J., Ding, D., Lin, Y., and Ma, Z. A versatile point cloud compressor using universal multiscale conditional coding – part i: Geometry. *IEEE Transactions on Pattern Analysis and Machine Intelligence*, 47(1):269–287, 2025a.
- Wang, K. and Gao, W. UniPCGC: Towards practical point cloud geometry compression via an efficient unified approach. *Proceedings of the AAAI Conference on Artificial Intelligence*, 39(12):12721–12729, Apr. 2025.
- Wang, M., Huang, R., Xie, W., Ma, Z., and Ma, S. Compression approaches for LiDAR point clouds and beyond: A survey. *ACM Transactions on Multimedia Computing, Communications and Applications*, 2025b.
- Wang, X., Xu, K., Deng, B., Guo, Y., and Wang, H. ASRL: Adaptive sparse representation learning for LiDAR point cloud geometry compression. *IEEE Signal Processing Letters*, 32:3884–3888, 2025c.
- Wang, X., Zhang, Y., Liu, T., Liu, X., Xu, K., Wan, J., Guo, Y., and Wang, H. TopNet: Transformer-efficient occupancy prediction network for octree-structured point cloud geometry compression. In *Proceedings of the IEEE/CVF Conference on Computer Vision and Pattern Recognition (CVPR)*, pp. 27305–27314, June 2025d.
- Wang, Y., Sun, Y., Liu, Z., Sarma, S. E., Bronstein, M. M., and Solomon, J. M. Dynamic graph CNN for learning on point clouds. *ACM Trans. Graph.*, 38(5), October 2019.
- WG 07 MPEG 3D Graphics Coding and Haptics Coding. G-PCC 2nd edition codec description. Output document N00575, ISO/IEC JTC1/SC29/WG7, 142th MPEG meeting, Antalya, 2023.
- WG 07 MPEG 3D Graphics Coding and Haptics Coding. Common test conditions for G-PCC. Output document N00944, ISO/IEC JTC1/SC29/WG7, 147th MPEG meeting, Sapporo, September 2024.
- Wu, X., Jiang, L., Wang, P.-S., Liu, Z., Liu, X., Qiao, Y., Ouyang, W., He, T., and Zhao, H. Point Transformer v3: Simpler faster stronger. In *Proceedings of the IEEE/CVF conference on computer vision and pattern recognition*, pp. 4840–4851, 2024.
- Wu, Y., Wang, Y., Zhang, S., and Ogai, H. Deep 3D object detection networks using LiDAR data: A review. *IEEE Sensors Journal*, 21(2):1152–1171, 2021.
- You, K., Chen, T., Ding, D., Asif, M. S., and Ma, Z. RENO: Real-time neural compression for 3D LiDAR point clouds. In *Proceedings of the IEEE/CVF Conference on Computer Vision and Pattern Recognition (CVPR)*, pp. 22172–22181, June 2025.
- Yu, P., Li, H., Jiang, R., Wang, J., Lin, L., and Guo, Y. Re-densification meets cross-scale propagation: Real-time neural compression of LiDAR point clouds. *arXiv preprint arXiv:2508.20466*, 2025.
- Zhang, W., Yang, F., Xu, Y., and Preda, M. Standardization status of MPEG geometry-based point cloud compression (G-PCC) edition 2. In *2024 Picture Coding Symposium (PCS)*, pp. 1–5. IEEE, 2024.

## A. Dataset Details

Four widely accepted datasets in LiDAR-related studies and standardization activities, including SemanticKITTI, Ford, nuScenes, and QNX, are used as training and evaluation in this work. A dataset overview is provided in the main manuscript. Here we detail the exact train/test splits for reproducibility, especially for nuScenes and QNX.

- **nuScenes.** We construct a fixed, scene-disjoint split, and deterministically sample frames within each scene. The nuScenes dataset is organized into ten subsets, each containing 85 scenes. For training, we extract the first 100 frames from the first 12 scenes in the first five subsets, resulting in 6,000 frames. For testing, we select the first 90 frames from the first scene of each of the last five subsets, yielding 450 frames.
- **QNX.** We follow the MPEG G-PCC CTC (WG 07 MPEG 3D Graphics Coding and Haptics Coding, 2024) sequences and adopt a sequence-level split. QNX contains four sequences: *Junction Approach* (74), *Junction Exit* (74), *Motorway Bridge* (811), and *Navigating Turns* (300) frames. We use *Motorway Bridge* and *Navigating Turns* for training, and *Junction Approach* and *Junction Exit* for testing.

We visualize typical samples from these datasets in Fig. 1.

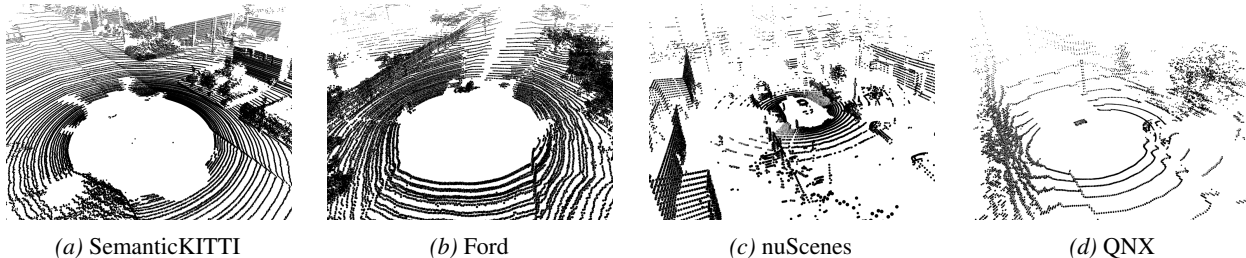


Figure 1. Visualization of samples in KITTI, Ford, nuScenes, and QNX LiDAR point cloud datasets.

## B. More Ablation Studies

### B.1. More Ablation Studies on Stage-Scalable Predictor

In our main manuscript, we conduct an ablation study on our stage-scalable predictor on the Ford (64-beam) dataset. In this supplementary material, we extend the cross-stage evaluation to two additional LiDAR datasets with different beam configurations: nuScenes (32-beam) and QNX (16-beam). The corresponding results are reported in Table 1 and Table 2. It is observed that our PACE exhibits a similar trend on Ford, nuScenes, and QNX. These ablation experiments sufficiently confirm the effectiveness of our stage-scalable predictor on diverse scenarios.

Table 1. On-the-fly reconfiguration of prediction stages on nuScenes (32-beam)

CONFIG	MEM. ↓	ENC. ↓	DEC. ↓	BD-BR ↓
1-STAGE	0.53GB	<b>0.58s</b>	<b>0.54s</b>	-39.77%
2-STAGE	0.53GB	0.60s	0.57s	-44.36%
4-STAGE	0.53GB	0.62s	0.62s	-46.82%
8-STAGE	0.53GB	0.68s	0.69s	-48.18%
16-STAGE	0.53GB	0.79s	0.90s	-48.98%
AUTOREGRESSIVE	0.53GB	6.61s	9.84s	<b>-50.38%</b>

### B.2. Weight Sharing for Stage-Scalable Predictors

We use a single predictor in PACE to support multiple coding modes. This design avoids maintaining a dedicated predictor head for each mode. In this section, we examine whether sharing predictor weights leads to any measurable loss in rate-distortion (R-D) performance, while highlighting the parameter savings.

To this end, we compare two training variants under the same data, optimizer, and training schedule; the only difference is whether predictor weights are shared. More specifically,

Table 2. On-the-fly reconfiguration of prediction stages on QNX (16-beam)

CONFIG	MEM. ↓	ENC. ↓	DEC. ↓	BD-BR ↓
1-STAGE	0.52GB	<b>0.33s</b>	<b>0.32s</b>	-50.82%
2-STAGE	0.52GB	0.34s	0.32s	-52.85%
4-STAGE	0.52GB	0.36s	0.34s	-53.94%
8-STAGE	0.52GB	0.39s	0.37s	-54.55%
16-STAGE	0.52GB	0.44s	0.48s	-54.87%
AUTOREGRESSIVE	0.52GB	3.27s	4.91s	<b>-55.18%</b>

Table 3. Ablation study on training strategy of stage-scalable predictor

CONFIG	INDIVIDUAL		JOINT	
	PARAM. ↓	BD-BR ↓	PARAM. ↓	BD-BR ↓
OURS-FP	10.00M + 0.57M × N	-50.68%	10.00M + 0.57M × 1	-50.19%
OURS-AR	10.00M + 0.57M × N	-55.93%	10.00M + 0.57M × 1	-55.07%

- (i) **Separate predictors:** the backbone is shared, while each supported mode configuration has its own predictor head;
- (ii) **Joint predictor:** a single predictor is shared across all modes (the method used in our PACE).

**Computational Complexity.** As summarized in Table 3, separate predictors increase the parameter count linearly with the number of supported configurations. Concretely, if the backbone has  $P_b$  parameters and each predictor head has  $P_p$ , then joint sharing uses  $P_b + P_p$ , whereas separate heads use  $P_b + P_p \times N$ , where  $N$  is the number of supported configurations. Apparently, the joint predictor largely saves parameters, which is significant for storage-sensitive tasks. Despite the additional capacity, the RD improvement from separate predictors is negligible: the joint predictor matches the separate-head setting closely across both FP and AR (the BD-BR gap remains very small). This indicates that a single conditioned predictor generalizes well across different stages and does not become the compression performance bottleneck when reconfiguring the number of stages at inference time.

**Compression Performance.** In terms of the coding performance, the joint predictor performs comparably to the separate predictors (e.g., -50.19% vs. -50.68 in FP and -55.07% vs. -55.93% in AR), although the separate predictors employ more parameters.

**Discussion.** A key practical advantage of the joint predictor is its cross-mode generalization capability. During training, we use a mixed-stage strategy in which the stage number  $S$  is sampled from a small subset (e.g.,  $S \in \{1, 2, 4, W\}$ ), and the same predictor is optimized across these configurations. Remarkably, at inference time, it generalizes effectively to much finer decompositions without noticeable R-D degradation. This indicates that a single learned predictor can generalize to different (including unseen) stage configurations without retraining, allowing on-the-fly reconfiguration at inference time.

Therefore, we adopt the joint predictor in PACE by default, as it simplifies deployment, maintains a stable model size and memory footprint as  $N$  grows, and achieves compression performance nearly identical to that of multiple specialized predictor heads.

### C. Special Case of Autoregressive Mode

In our framework, the AR mode is a special case in terms of implementation. For a general  $S$ -stage decoding strategy, we run the backbone once per window (window length  $W = 1024$ ), and then invoke the stage-scalable predictor once per stage, each time performing full-window inference. A naive AR realization under this pipeline would still require  $W$  predictor calls per window, which is computationally prohibitive. In our implementation, a full-window backbone pass takes  $\sim 6$  ms, while a single predictor call takes  $\sim 0.3$  ms; thus, even with only one backbone execution,  $1024 \times$  predictor invocations per window lead to excessive latency.

To accelerate AR, we further reduce its overhead by leveraging Mamba’s step inference. Specifically, step inference exposes a stateful token-by-token interface: instead of recomputing a full window forward pass for each prediction, the model maintains recurrent states and updates them incrementally so that each step consumes a context of length 1 and produces the

next-symbol distribution. This converts AR decoding into a streaming process with stable per-token cost, and the resulting throughput corresponds to the AR speed reported in our paper.

In principle, the encoder could further exploit parallelism because the full octree information is known in advance, allowing the predictor to be evaluated in a vectorized manner (the same as the throughput of the one-stage mode). However, entropy coding requires the encoder and decoder to use exactly the same probability outputs in the same order; even tiny floating-point deviations (e.g., due to GPU non-associativity, different kernel fusion/reduction orders, or nondeterministic execution) can lead to mismatched cumulative frequencies and thus break encoder-decoder synchronization. In our experiments, we observed that such “near-identical” probabilities under parallel encoding can still be unsafe for strict bit-exact arithmetic coding. Therefore, to guarantee bitstream correctness, we enforce a symmetric implementation and use the same step-inference path for both encoding and decoding, i.e., our encoder is implemented to sequentially rather than in parallel to process nodes in AR. Therefore, our encoding time is rather long in the AR mode.

It is possible to recover safe encoder-side parallelism by further discretizing the probability model, e.g., via quantization or fixed-point implementations with explicit rounding, so that the predicted distributions become bit-exact across execution orders and hardware backends. We leave this direction for future work.

### D. Comparison with Predtree-based Methods

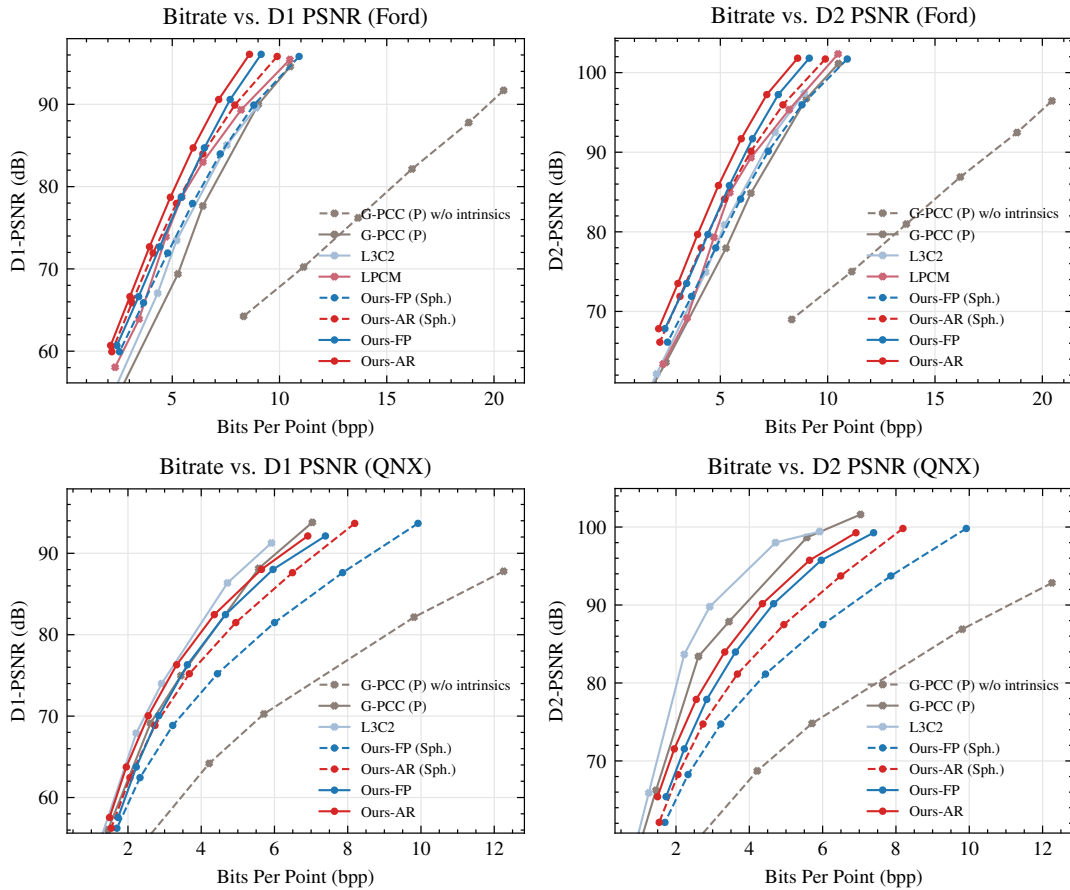


Figure 2. Comparison with predtree-based methods on Ford and QNX. G-PCC (P) represents G-PCC (Predgeom) in the figures.

Predtree-based methods, especially rules-based ones, typically rely on accurate LiDAR intrinsics for prediction-tree construction. They are more effective on intrinsics-provided datasets and can outperform octree-based methods under these conditions (e.g., Ford and QNX). However, as shown in Fig. 2, by incorporating intrinsic-aware preprocessing, PACE equips the octree with the ability to leverage intrinsic data, leading to substantial compression improvements in these scenarios.

**Discussion on QNX.** Further, we observe in Fig. 2 that G-PCC (Predgeom) and L3C2 attain slightly higher coding



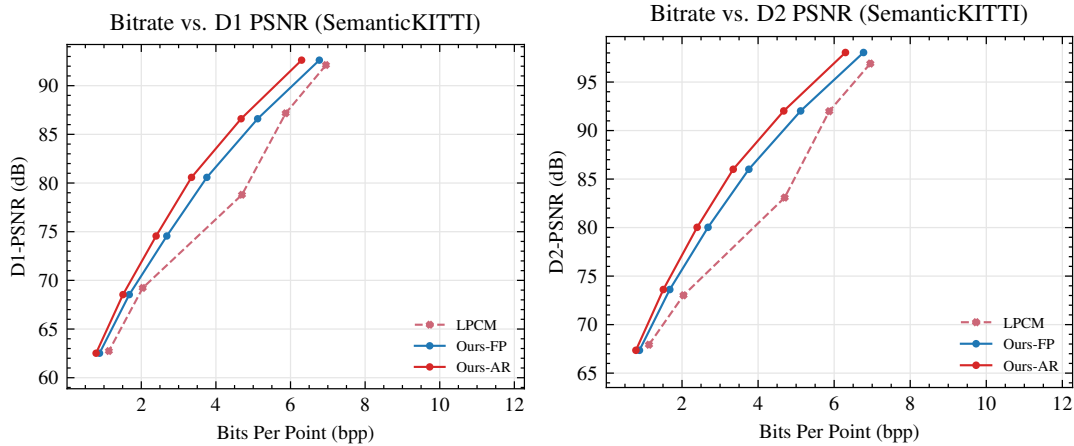


Figure 3. Comparison with learning-based predtree method LPCM on SemanticKITTI.

Notably, LPCM adopts a two-branch design to handle different bitrates. As evidenced by the R-D curves, it exhibits a clear breakpoint, which is induced by switching between two coding branches across the high- and low-bitrates. In the high bitrates, LPCM follows a predtree-style predictive coding pipeline. In the low bitrates, however, LPCM switches to an autoencoder branch. This is because when the underlying geometric priors are weak or noisy (e.g., under missing/unreliable intrinsics), predictive coding becomes brittle at low bitrates, and the overall R-D behavior may deteriorate sharply.

By contrast, our PACE adopts a monolithic solution to cover a wide bitrate range. It can be observed from Fig. 2 and Fig. 3 that PACE consistently outperforms LPCM at all bitrate points on both Ford and SemanticKITTI. Since LPCM only provides results on these two datasets, we cannot compare with it on more datasets like QNX and nuScenes.

### E. Qualitative Results

We visualize the LiDAR point cloud reconstructed by different methods in Fig. 4 for subjective quality assessment.

### F. Limitations

As shown in Table 4 of the main manuscript and Tables 1 and 2 of this supplementary material, the encoding time of our autoregressive mode is much longer than that of other modes. This speed could be further improved, as all required information is available at the encoder and parallel processing is feasible. However, as discussed in Section C, implementing such parallelism would require techniques such as quantization and hardware optimization, which are beyond the scope of this work. Future work will focus on optimizing PACE for faster encoding.

Currently, PACE does not meet real-time processing requirements. Future work will focus on accelerating its coding speed through efficient attention networks, model distillation, and other techniques, while preserving compression performance as much as possible.

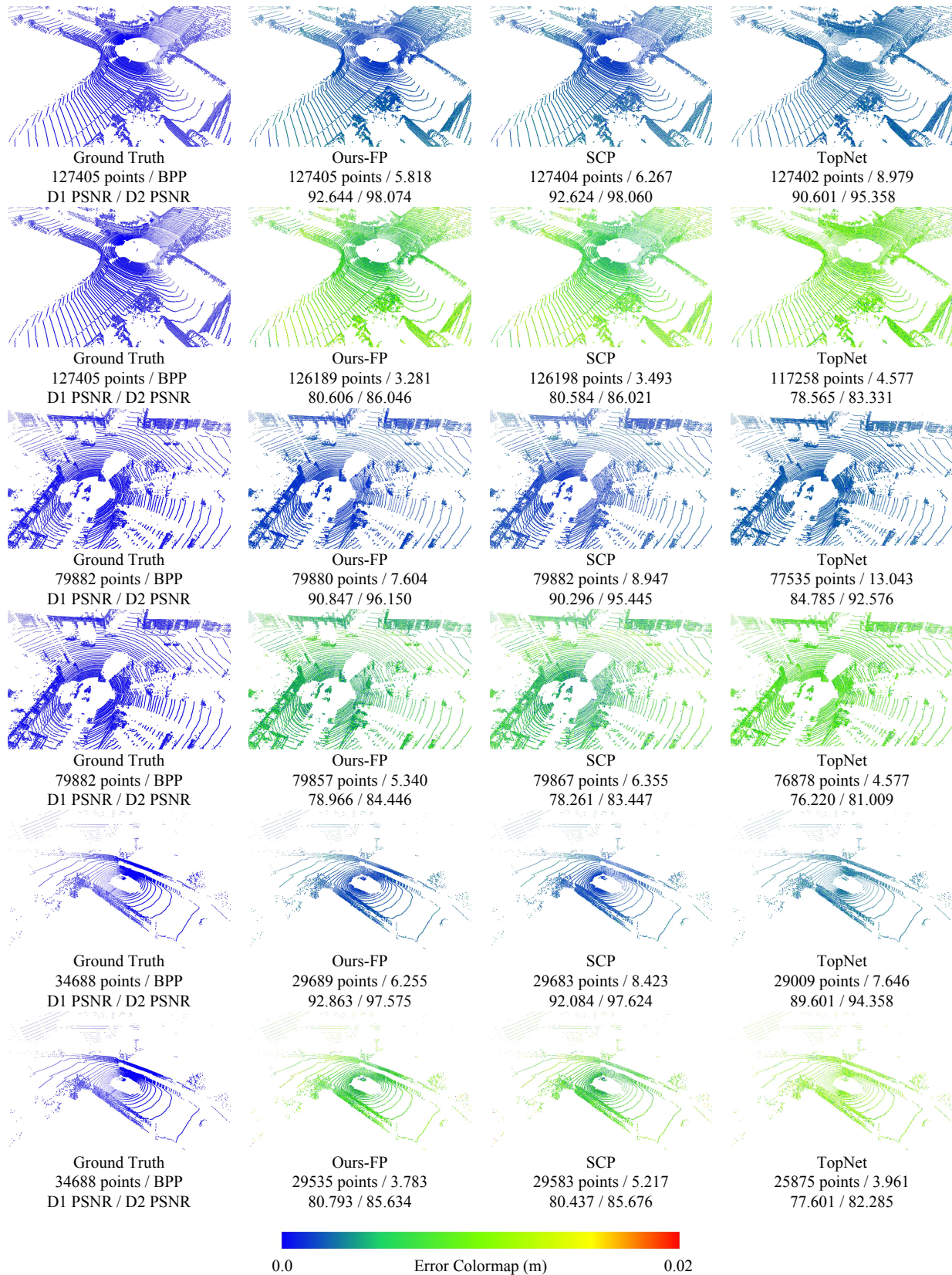


Figure 4. Qualitative visualization. Rows 1, 3, and 5 present compression results at higher bitrates, while Rows 2, 4, and 6 show results at lower bitrates. Representative samples from SemanticKITTI (Rows 1-2), Ford (Rows 3-4), and nuScenes (Rows 5-6) are shown.